Research Article

Optimizing Aerosolization Using Computational Fluid Dynamics in a Pediatric Air-Jet Dry Powder Inhaler

Karl Bass,[1] Dale Farkas,[1] and Worth Longest[1,2,3]

Abstract. The objective of this study was to optimize the performance of a high-efficiency pediatric inhaler, referred to as the pediatric air-jet DPI, using computational fluid dynamics (CFD) simulations with supporting experimental analysis of aerosol formation. The pediatric air-jet DPI forms an internal flow pathway consisting of an inlet jet of high-speed air, capsule chamber containing a powder formulation, and outlet orifice. Instead of simulating full breakup of the powder bed to an aerosol in this complex flow system, which is computationally expensive, flow-field-based dispersion parameters were sought that correlated with experimentally determined aerosolization metrics. For the pediatric air-jet DPI configuration that was considered, mass median aerodynamic diameter (MMAD) directly correlated with input turbulent kinetic energy normalized by actuation pressure and flow kinetic energy. Emitted dose (ED) correlated best with input flow rate multiplied by the ratio of capillary diameters. Based on these dispersion parameters, an automated CFD process was used over multiple iterations of over 100 designs to identify optimal inlet and outlet capillary diameters, which affected system performance in complex and unexpected ways. Experimental verification of the optimized designs indicated an MMAD < 1.6 μm and an ED > 90% of loaded dose. While extrathoracic depositional loss will be determined in future studies, at an operating flow rate of 15 L/min, it is expected that pediatric mouth-throat or even nose-throat aerosol deposition fractions will be below 10% and potentially less than 5% representing a significant improvement in the delivery efficiency of dry powder pharmaceutical aerosols to children.

KEY WORDS: active dry powder inhaler; small particle aerosol; inline dry powder inhaler; high-efficiency aerosolization; aerosol delivery to children.

INTRODUCTION

In the field of respiratory drug delivery, computational fluid dynamics (CFD) is proving to be an increasingly useful tool for the development and optimization of dry powder inhalers (DPIs). For example, in a series of papers, Coates *et al.* used CFD to investigate the effects of mouthpiece length and grid design (1), capsule size (2), flow rate (3), air inlet size (4), and mouthpiece geometry (5) on DPI performance in terms of capsule, device, and extrathoracic losses. More recently, Shur *et al.* (6) modified the air inlets of a Cyclohaler, guided by CFD analysis, to match the aerosolization performance of the HandiHaler.

Our group has developed a series of high-efficiency air-jet DPIs that are operated with 10 ml of air (*via* a syringe) (7–9). These air-jet DPIs use small-gauge hollow capillaries that pierce a powder-containing capsule as part of loading the device and serve as the air inlet and aerosol outlet. The inlet capillary supplies a high-velocity, compressible, turbulent jet that initially fluidizes the powder bed. It is expected that significant turbulence and high shear forces further break up the initially formed aggregates, which reduces the particle size while in the capsule chamber (8,9). Once the size of an aerosolized aggregate is sufficiently reduced, it is able to escape the powder chamber through the outlet capillary and enter the patient interface.

A detailed approach to modeling DPI aerosolization and transport in CFD could utilize Lagrangian particle tracking (8,9) or discrete element modeling (DEM) (10–12) as a representation of the powder. However, these models become computationally expensive when a complete device and powder dose need to be simulated in order to make design

[1] Department of Mechanical and Nuclear Engineering, Virginia Commonwealth University, 401 W Main Street, PO Box 843015, Richmond, Virginia 23284, USA.
[2] Department of Pharmaceutics, Virginia Commonwealth University, 401 West Main Street, P.O. Box 843015, Richmond, Virginia 23284-3015, USA.
[3] To whom correspondence should be addressed. (e–mail: pwlongest@vcu.edu)

improvement predictions. For example, current DEM simulations that attempt to capture powder structural properties with particle-particle and particle-wall interactions are currently limited to one or two particle agglomerates (13,14). In contrast, an effective approach for predicting the aerosolization behavior of a DPI is to develop predictive correlations that relate dispersion parameters, which use CFD-predicted flow and turbulence quantities, to aerosolization performance metrics (3,6,8,9).

Specific to the air-jet DPI development in the current study, Longest and Farkas (8) developed quantitative flow-field-based and tracer-particle-based correlations that related device aerosolization to flow and turbulence *dispersion parameters* for a very low volume of actuation air (*i.e.* 10 mL). The tracer-particle method used a relatively small number of Lagrangian particles, compared to modeling the entire powder bed, to sample turbulence and flow quantities throughout the domain. To quantify device performance, the aerosolization metrics of mass-median aerodynamic diameter (MMAD) and emitted dose (ED) (also often referred to as emitted fraction) were used. Their study showed that MMAD had a strong direct correlation ($R^2 > 0.8$) with two flow-field-based dispersion parameters, which were a non-dimensional form of turbulent kinetic energy (k), denoted by k^*_{field}, and the product of non-dimensional k and non-dimensional specific dissipation rate (ω), denoted by $k^*_{field} \times \omega^*_{field}$. The ED also showed a strong correlation with k^*_{field} and $k^*_{field} \times \omega^*_{field}$, as well as $k^*_{field}/\omega^*_{field}$ and wall shear stress (WSS). The predictive capabilities of these correlations were evaluated by Longest *et al.* (9) by comparing the predicted MMAD and ED from CFD models to experimental results *a priori*, with results showing a low root-mean-square (RMS) error (again, for a 10 mL actuation air volume). The findings from these two studies demonstrated that dispersion parameters can be correlated to be predictive of MMAD and ED performance for air-jet DPIs. They also suggested that the powder goes through a two-stage aerosolization process, where the first stage involves the initial dispersion from the stationary powder bed to the flow field, followed by secondary breakup in the high-velocity, highly turbulent air jet.

The present study builds upon the previous development of a high-efficiency inline air-jet DPI and applies this platform to the delivery of tobramycin to children with cystic fibrosis (*CF*). A primary symptom of *CF* is dehydration of the airway surface liquid in the lungs, due to poor ion transport through epithelial cells (15,16), which produces thickened mucus and poor mucociliary clearance (17). Poor lung clearance and abnormal ion concentrations lead to frequent bacterial infections, the most predominant of which is *Pseudomonas aeruginosa* (*Pa*) (18), which can be treated by inhaled antibiotics. Tobramycin was the first commercial inhaled antibiotic (19) and is available as either a solution or powder for nebulizers or DPIs, respectively. The efficacy of treating *Pa* infections with tobramycin was demonstrated in a clinical trial by Ramsey *et al.* (20) who reported an average 12% increase in FEV_1 (forced expiratory volume over 1 s), 26% decrease in pulmonary exacerbations, less hospitalization, and a 1.1 log_{10} CFU/g reduction in *Pa* infection.

Our group is developing a pediatric DPI for the administration of spray-dried excipient enhanced growth (EEG) powder formulation to children with *CF* as young as 2 years old. As described by Farkas *et al.* (21), the delivery system is intended to provide the aerosol and a full inhalation through either a sealed nasal cannula or mouthpiece interface. By delivering a full inhalation from a positive pressure gas source, the device has multiple advantages compared with typical passive DPIs including consistent actuation, the flexibility of oral or nasal lung delivery, potential expansion of the upper airways, and resistance to exhalation through the device. The study of Farkas *et al.* (21) previously established that improved aerosolization was achieved when all of the available gas flow was passed through the powder chamber. To achieve the much higher flow rates (~ 15 LPM) compared with the previous studies of Longest and Farkas (8) and Longest *et al.* (9) (~ 3 LPM), capillary diameters were increased, which alters the turbulence and shear stress profiles within the device. As a result, aerosolization characteristics and dispersion parameters are expected to be considerably different for the current pediatric devices compared with the previous devices that were operated with 10 mL of actuation air.

The proposed pediatric device for tobramycin uses an inline, positive-pressure actuation and air-jet aerosolization. Specifically, a standard ventilation bag is connected to the inlet, which provides the actuation air volume (~ 750 mL) and a pressure drop (~ 6 kPa) across the device. The inlet capillary then supplies a high-velocity, highly turbulent air jet to the capsule chamber to aerosolize the powder. Initial devices are developed for patients in the age ranges of 2–3, 5–6, and 9–10 years old and aim to provide the inhalation volume for one breath as part of the actuation process. The present study focuses on the 5–6-year-old group, with a target inhalation volume of 750 mL and total device air flow rate of 15 LPM.

Experimental aerosolization performance from four prototyped versions of the proposed pediatric air-jet DPI were presented by Farkas *et al.* (21) which forms the basis of correlation development for the current study. The minimum device aerosolization performance goals of the experimental study were an ED > 85% (of loaded dose), MMAD < 1.75 μm, fine particle fraction of ED < 5 μm ($FPF_{<5\mu m/ED}$) > 90%, and $FPF_{<1\mu m/ED} > 20\%$, all of which were achieved by the case 4 device ($FPF_{<1\mu m/ED}$ was 19.5%). Considering aerosol administration through *in vitro* airway models of a 5-year-old child, the case 4 device delivered 60.7% to the tracheal filter, with 8.3% nose-throat losses, when coupled to the best case nasal cannula design; and 63.8% to the tracheal filter, with 6.6% mouth-throat losses, when coupled with the best case mouthpiece design. This is a marked improvement over the typical DPI performance for aerosol administration to children that is reported in the literature. Specifically, for oral aerosol delivery to a 4–5-year-old *in vitro* model, Below *et al.* (22) reported 5% and 22% of nominal dose deposited on the tracheal filter with the Novolizer and Easyhaler; and Lindert *et al.* (23) reported 9% to 11% lung delivery efficiency with the Cyclohaler, HandiHaler, and Spinhaler. For trans-nasal aerosol delivery to children in the age ranges considered, little data is available in the literature. The closest available study is Laube *et al.* (24) who reported < 4% of loaded dose delivered to the tracheal filter in the 9-month-old *in vitro* SAINT model (25).

The objective of this study was to implement CFD simulations to develop quantitative correlations that predict the aerosolization behavior of an inline air-jet DPI for children and then use these correlations to optimize aerosolization performance. In order to develop the flow-field based correlations for aerosolization performance, CFD simulations of four initial devices were conducted and compared with the previous experimentally determined aerosolization metrics reported by Farkas *et al.* (21). Based on these findings, a second iteration of designs was developed and tested both experimentally and with the evolving CFD model. The complete set of ten devices was then used to identify the best CFD-based dispersion parameters for predicting MMAD and ED in the pediatric air-jet DPIs. These dispersion parameters were then used to develop a CFD optimized design for improved performance with increased ED and reduced MMAD compared with previous studies. As a final step, the best case designs were produced and tested experimentally to validate the CFD predictions and optimization method.

MATERIALS AND METHODS

The current study builds upon the initial experimental work with pediatric air-jet DPIs presented by Farkas *et al.* (21), and the devices and results from that study are referred to as experimental iteration 1. In the current study, CFD models were developed for the devices in experimental iteration 1 and initial CFD dispersion parameters were calculated based on our previous work with low (~ 10 mL) actuation volumes (8,9). A second round of pediatric air-jet devices was then prototyped and tested experimentally, which is referred to as experimental iteration 2. New dispersion parameters, which are appropriate for the higher flow volumes of the pediatric air-jet DPIs (~ 750 mL), were then developed for both device sets (experimental iterations 1 and 2) and compared with the experimental data to determine their ability to predict ED and MMAD. Device optimization then begins by evaluating numerous design configurations with CFD and using the refined dispersion parameters to estimate performance. The entire experimental, CFD, and optimization approach is described in detail in the following sections.

Optimization Process

To meet the objective, the device optimization process is outlined by the block diagram in Fig. 1. This process utilizes concurrent experimental and CFD models to provide physical insight into aerosolization performance, and iterations through the process aim to refine the dispersion parameters and optimize the device performance. The overarching aims of the process are to (i) provide an *a priori* validation of CFD-based dispersion parameter predictions of aerosolization performance and (ii) determine the best performing device parameters within the design space.

The *Initial Device Development* stage (Fig. 1) is largely covered by the work presented in our previous publications on pediatric air-jet DPI development (8,9,21). Here, the initial air-jet DPI concept was developed with a combination of analytical, experimental, and numerical methods. Fabrication of prototype air-jet DPIs uses computer-aided design (CAD) models and 3D printing for the plastic components, with small gauge stainless steel hollow tubes used for the inlet and outlet capillaries. Once prototype devices are built, the *Aerosolization Experiments* stage tests the aerosolization performance (MMAD and ED) of the DPI. The experimental setup uses a next-generation impactor (NGI) and high-performance liquid chromatography (HPLC) to determine the particle size distribution and capsule retention, both of which are used to establish performance metrics. In parallel to the *Aerosolization Experiments* stage, the *CFD Evaluation* stage uses numerical models to provide insight into the flow and turbulence conditions within the devices. It is expected that numerous CFD simulations will be conducted during the optimization process (over 100 design configurations), so the geometry, meshing, model set-up, and post-processing steps are automated as much as possible. In the *Correlation Development* stage, the flow and turbulence quantities from the CFD simulations are used to identify and develop dispersion parameters that are predictive of the aerosolization performance metrics.

After predictive correlations are developed, the process loops back through the *Aerosolization Experiments* and *CFD Evaluation* stages to test the correlations for accuracy and develop insights into newly defined dispersion parameters (see Iteration 2 in Fig. 1). Following correlation development and testing, it is important to evaluate how changes to the device design influence the dispersion parameters and associated aerosolization performance predictions. The flow and turbulence quantities from CFD models of numerous design configurations are evaluated to determine trends between design factors and device flow characteristics. These quantities are then used in the dispersion parameters and correlations to provide predictions of aerosolization performance. Finally, the predictions of aerosolization performance from the previous stage are used to identify optimized device designs. The optimized device should both provide good aerosolization performance and be an improvement over the devices from experimental iteration 1. *A priori* validation of the CFD predictions is conducted by producing and experimentally testing the optimized devices to determine whether the aerosolization performance predictions are accurate, without making adjustments to the models or correlations after the simulations are conducted.

Experimental Materials and Powder Formulation

Albuterol sulfate (AS) USP was purchased from Spectrum Chemicals (Gardena, CA) and Pearlitol® PF-Mannitol was donated from Roquette Pharma (Lestrem, France). Poloxamer 188 (Leutrol F68) was donated from BASF Corporation (Florham Park, NJ). L-leucine and all other reagents were purchased from Sigma Chemical Co. (St. Louis, MO). Quali-V, Hydroxypropyl methylcellulose (HPMC) capsules (size 0) were donated from Qualicaps (Whitsett, NC).

Multiple batches of a spray-dried AS EEG powder formulation were produced based on the optimized method described by Son *et al.* (26,27) using a Büchi Nano spray dryer B-90 (Büchi Laboratory-Techniques, Flawil, Switzerland). The EEG powder formulation contained a 30:48:20:2% *w/w* ratio of AS, mannitol, L-leucine, and Poloxamer 188.
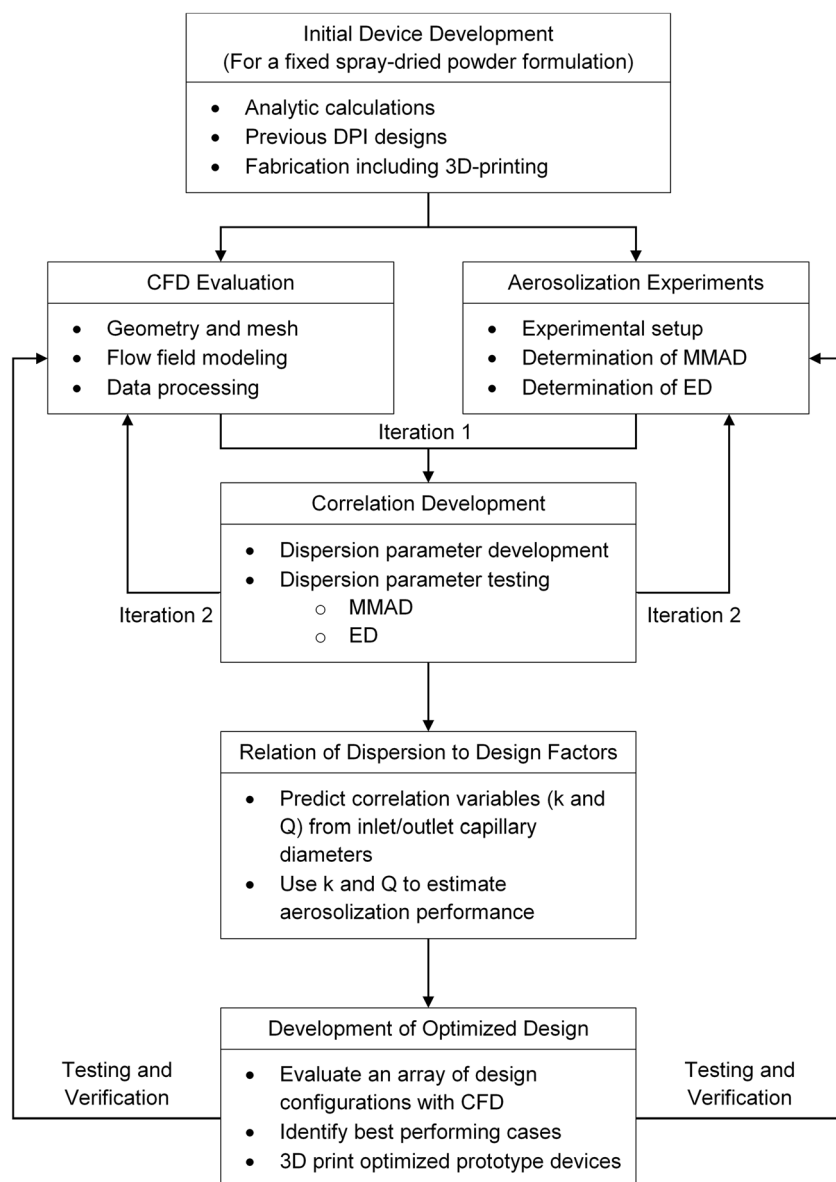
Fig. 1. Block diagram of device development and optimization process

Device Design and Experimental Methods

The devices that were tested in experimental iterations 1 and 2, along with their inlet and outlet diameter configurations and operating conditions are summarized in Table I. The naming convention for cases in experimental iteration 2 (Table I) gives the inlet capillary diameter followed by the outlet capillary diameter, as that is the primary design factor that was evaluated. For example, a case called 1.83/2.90 uses a 1.83-mm inlet diameter and a 2.90-mm outlet diameter, and all other design factors and operating conditions are the same as cases 3 and 4 in experimental iteration 1. This includes an operating inlet pressure of 6 kPa, which is easily generated with one hand operation of a pediatric size ventilation bag (21). The half Q case is the exception to this naming convention as it is the same device as case 4, but implements a pressure drop of 1.5 kPa to reduce the flow rate through the device by a factor of two. The 1.32/2.39 case used the same outlet capillary diameter and pressure drop as case 4, but included a 1.32-mm inlet capillary to increase flow resistance and give a similar flow rate to the half Q case. Likewise, the 1.60/2.39 case used a 1.60-mm inlet capillary to give a flow rate that was approximately 75% of case 4. The 2.08/2.69 case has a similar outlet to inlet diameter ratio (d_o/d_i) as case 4 (*i.e.*, ~ 1.30). The 1.32/2.90 case has the same average capillary diameter ($0.5 \times (d_i + d_o)$) as case 4 (*i.e.*, 2.11 mm) and tests an example where the outlet diameter is much larger than the inlet. Finally, the 3.00/2.08 case tests the influence of having a larger inlet compared to the outlet diameter, and maximizes the flow rate (and hence available flow energy) through the device.

Details on the device design and experimental methods for experimental iteration 1 are discussed in depth by Farkas *et al.* (21). The additional experimental work carried out for experimental iteration 2 in the present study followed the same device design, operation, and methods as experimental iteration 1. In brief, a size 0 HPMC capsule was loaded with 10 mg of AS EEG powder formulation, and the device used

Table I. Summary of Experimentally Tested Device Configurations and Operating Conditions

	d_i (mm)	d_o (mm)	Bypass	ΔP (kPa)	Q (LPM)	Notes
Experimental iteration 1						
Case 1[a]	1.52	1.52	Yes	6.0	11.4	Bypass flow with same diameter inlet and outlet capillaries
Case 2[a]	1.40	1.80	Yes	6.0	11.6	Bypass flow with smaller inlet than outlet capillary
Case 3[a]	2.39	2.39	No	6.0	17.4	No bypass flow with same diameter inlet and outlet capillaries
Case 4[a]	1.83	2.39	No	6.0	13.3	No bypass flow with smaller inlet than outlet capillary, but same outlet as case 3 (best performing case of experimental iteration 1)
Experimental iteration 2						
Half Q	1.83	2.39	No	1.5	6.7	Pressure drop selected to give 50% of case 4 flow rate
1.32/2.39	1.32	2.39	No	6.0	5.9	Inlet diameter selected to give 50% of case 4 flow rate
1.60/2.39	1.60	2.39	No	6.0	9.9	Inlet diameter selected to give 75% of case 4 flow rate
2.08/2.69	2.08	2.69	No	6.0	16.9	Similar outlet to inlet diameter ratio as case 4
1.32/2.90	1.32	2.90	No	6.0	6.8	Same average capillary diameter as case 4
1.32/2.90	3.00	2.08	No	6.0	15.5	Explores the effect of larger inlet compared to the outlet diameter

[a] Results presented by Farkas *et al.* (21)

hollow capillaries to pierce the capsule when the device was closed with a single twisting action. Actuation of the device passes a high velocity air jet through the inlet capillary, which aerosolizes the power, and the particles leave the capsule *via* the outlet capillary leading to the patient interface. In the present study, the only design factors that were manipulated were the inlet and outlet capillary diameters. Design factors that were kept constant included the insertion length of the capillary in the capsule, capsule size, piecing angle, piercing location (along the long axis of the capsule), and a horizontal orientation of the device. Preliminary experimental work considered angling the inlet capillary relative to the outlet capillary, similar to case 7 in the Longest *et al.* study (9), in an effort to increase secondary flow, but there was little improvement in aerosolization performance. Similarly, preliminary work extended the outlet capillary length in an effort to expose the aerosol to high shear flow for a longer duration, but again there was no improvement in MMAD or ED compared with experimental iteration 1. Figure 2a shows a rendering of the case 4 device in transparent plastic, with the capsule and capillaries clearly visible. Figure 2b shows the internal flow path, which represents the computational domain for CFD models, and the height to which the 10 mg powder bed fills the capsule.

All devices were actuated with a 6 kPa pressure drop (with the exception of the half Q case) *via* a compressed air line and solenoid valve. Previous results indicated very similar device performance with either a hand-operated ventilation bag or compressed air and solenoid valve setup (21). Inlet flow rate through each device was recorded before loading a capsule, and the time of actuation (controlled by the solenoid valve) was adjusted to ensure that 750 ml passed through the device, which is consistent with a deep inhalation volume for a 5–6 year old child (75% of total lung capacity) (28). The aerosol characterization was performed using a NGI and AS drug mass was quantified using HPLC, with the device actuated into the NGI using a custom adaptor. After actuation, HPLC was used to determine recovered drug masses in the capsule and device, and the amount of powder that deposited on each stage of the NGI. As minimal size

change is expected in the aerosol under ambient temperature and relative humidity (RH) conditions, experiments were conducted with ambient air (T = 22°C ± 3°C and RH = 50% ± 5%) with the NGI at room temperature. AS quantification was performed with a validated HPLC method using a Waters 2695 separations module with a 2475 fluorescence detector (Waters Co., Milford, MA). Chromatography was performed using a Restek Allure PFP 150 mm × 2.1 mm column (Bellefonte, PA). The mobile phase, consisting of methanol and ammonium formate buffer (20 mM, pH 3.4) in a ratio of 70:30, respectively, was eluted at a flow rate of 0.4 mL/min and the detector was set to an excitation wavelength of 276 nm and emission at 609 nm. The column temperature was
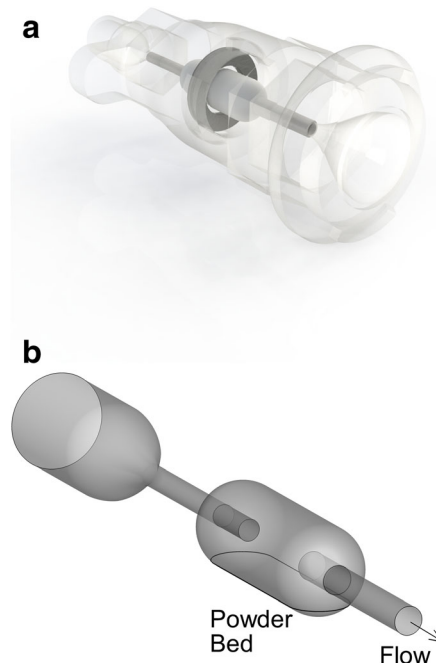

Fig. 2. Overview of device geometry showing **a** CAD rendering with inlet and outlet connections, stainless steel capillaries, size 0 capsule, and rubber O-ring. **b** Internal flow pathway used for the CFD domain

maintained at 25°C, and the volume of each sample injected was 10 μL. The limit of quantification was 0.5 μg/mL [26,29]. The recovered dose from HPLC analysis for all experimental data presented in this study was greater than 90%.

The ED was defined as the difference between the loaded AS dose and the mass of AS retained in the capsule and device after one actuation, divided by the loaded dose, and expressed as a percentage. The MMAD was identified with linear interpolation of a cumulative percentage drug mass *vs.* cutoff diameter plot from the NGI. The cutoff diameters of each NGI stage were calculated using the formula specified in USP 35 (Chapter 601, Apparatus 5) for the operating flow rate of 45 LPM. The exception in the present study is that the higher flow rate of some devices required the NGI to be operated at a flow rate of 60 LPM. To account for this when determining the MMAD for these devices, the cutoff diameters were recalculated using the formula from USP 35 for a flow rate of 60 LPM.

CFD Models

The computational domains and meshes were generated according to our previously established best practices [30–32]. Meshes were composed of very high quality hexahedral cells, with orthogonality greater than 0.25, and followed a similar construction style as our previous air-jet DPI studies [8,9]. To reduce the time required for CFD model development, geometry and mesh generation were automated as much as possible using an input file with design parameters and automation scripts, as it was expected that numerous design configurations would be explored during the optimization process. This automation reduced the time to create each mesh from approximately an hour of repetitive manual work to less than 2 min, and minimized the possibility of human error. To confirm mesh independent results, CFD quantities specific to flow, turbulence, and compressibility were evaluated for a coarse (230,208 cells), medium (496,128 cells), fine (976,000 cells), and extra fine (2,044,588 cells) mesh that represented the case 4 device configuration, with mesh independence established between the fine and extra fine mesh. Between these two meshes, the volume-averaged velocity magnitude had an absolute difference of -0.05 m/s (-0.30% relative difference), the volume-averaged turbulence kinetic energy had an absolute difference of -0.02 m^2/s^2 (-0.19% relative difference), and the inlet and outlet volumetric flow rates had an absolute difference of -0.102 LPM and -0.103 LPM, respectively (-0.54% and -0.53%, respectively). This mesh resolution is also consistent with the cell counts used in our previous air-jet DPI CFD work [8,9].

For experimental iteration 1, cases have inlet boundary Mach and Reynolds numbers ranging from 0.18 to 0.27 and 6300 to 13,200, respectively. These cases are below the recommended Mach number threshold of 0.3 for compressible flow, but the ideal gas law for density modeling was implemented to be consistent with previous DPI studies [8,9] and to ensure CFD models are capable of handling higher inlet velocity if the flow rate is increased during optimization. Based on inlet Reynolds numbers, some cases exhibit highly turbulent behavior, and at the very least flow is beyond the transitional regime. As such, the low-Reynolds number (LRN) k-ω turbulence model was implemented, which has been extensively validated for drug delivery applications by our group [30,33,34] and was shown to give a good compromise between computational accuracy and efficiency. Despite very high inlet Reynolds numbers, the LRN correction was applied to account for the possibility of low turbulence regions within the domain, particularly at locations far from the inlet capillary jet. The form of the LRN corrections makes the model applicable to both high and low turbulence regions, as the eddy viscosity damping coefficient approaches unity in regions of high turbulence and hence has little effect. Based on the presence of a high velocity inlet jet and compressible flow, shear flow corrections and compressibility effects were also implemented [35].

Consistent with our previous air-jet DPI CFD studies [8,9], a steady-state approach for transport equation discretization would not provide a converged solution due to the presence of relatively high frequency (~ 1000 Hz) flow oscillations. As such, the CFD model used a partially converged steady-state solution as the initial condition, then switched to a transient approach, with a time step of 1e-4 s that provided good convergence and accurately resolved the flow oscillations. Differences between volume-average flow and turbulence quantities were observed to be negligible after approximately 100 time steps, suggesting that start-up effects had dissipated. As dispersion metrics are based on volume-average quantities, it is expected that this solution strategy will be capable of providing predictive correlations, as was the case when a similar approach was implemented by Longest and Farkas [8].

Both flow-based and particle-based dispersion parameters were originally presented by Longest and Farkas [8], which demonstrated the predictive capabilities of CFD models for DPI aerosolization performance. The former used volume-averaged flow and turbulence quantities as the basis of the dispersion parameters, and the latter used tracer particles to sample flow and turbulence quantities as their trajectories moved from the powder bed and through the domain. As both flow-based and particle-based dispersion parameters performed well in previous studies, the current study will analyze an extended set of flow-based parameters, which reduces overall processing time.

All flow and turbulence transport equations were solved using ANSYS Fluent v19.0, including the necessary sub-models and corrections described previously. CFD models adhered to the recommended guidelines presented by Bass and Longest [30], in particular the implementation of the Green-Gauss Node-based method for gradient discretization. Spatial discretization of transport equations, including k and ω, were second-order accurate. Convective terms used a second-order upwind scheme and diffusion terms used central difference. Further details on the mass, momentum, and turbulence transport equations are available in other publications [36,37]. As with the meshing stage of CFD model development, the setup in ANSYS Fluent that was required for each case was automated as much as possible by utilizing the scripting capabilities of the Fluent text user interface.

In all experimental runs, the DPI was activated by applying a 6 kPa pressure drop across the device. The CFD

models implement this pressure gradient with a pressure inlet boundary condition set to 6 kPa and a pressure outlet boundary condition set to 0 kPa, with all pressures given as gauge pressure. The pressure difference between the inlet and outlet boundary drives flow through the computational model, and the device geometry determines flow resistance and hence the volumetric flow rate. As an initial validation check of both the model selection and boundary conditions, the inlet flow rate between CFD models and available experimental flow rate data was compared to ensure the numerical results were similar to the actual devices. On average, the absolute difference between CFD and experimental flow rate differed by approximately 1 LPM, or a relative difference of 6%. Generally, the CFD over-predicted flow rate compared to the experimental results, which can be attributed to the surface roughness of plastic components increasing flow resistance and minor simplifications of the geometry in the CFD model.

Dispersion Parameters

The CFD-predicted dispersion parameters used in the current study and previous work by our group (8,9) use flow and turbulence quantities to characterize the conditions that drive powder aerosolization within in the pediatric air-jet DPI. Flow quantities are generally ubiquitous and well understood across all scientific fields, such as inlet flow velocity, but turbulence quantities are less common in fields outside of CFD, such as turbulent kinetic energy (k) and specific dissipation rate (ω). In turbulence modeling, the flow velocity is typically decomposed into time-averaged and fluctuating components. The time-averaged component is the mean flow through the domain and is represented by $\overline{u}$, $\overline{v}$, and $\overline{z}$ in the x-, y-, and z-directions, respectively. The fluctuating velocity component represents the random and chaotic instabilities that the turbulent eddies contribute to the flow and is represented by u', v', and w' in the x-, y-, and z-directions, respectively. The combination of mean (time-averaged) and fluctuating velocity components provides the instantaneous flow field velocity, *i.e.* $u = \overline{u} + u'$. Turbulent kinetic energy (k) is the specific energy (per unit mass) that turbulence contributes to the total flow field energy, and is defined as (35):

$$k = \frac{1}{2}\left(\overline{u'^2} + \overline{v'^2} + \overline{w'^2}\right) \tag{1}$$

with units (m^2/s^2). A common analogy to describe the mean and fluctuating velocity components is to consider a probe that samples instantaneous velocity at a single point in a turbulent flow. The resultant sampling trace would show erratic oscillations in velocity against time. In this case, the mean velocity ($\overline{u}$, $\overline{v}$, and $\overline{z}$) would be the time-averaged value of the oscillations, and the fluctuating component is the difference between the instantaneous and mean velocity across any given time integration (38).

The second modeling quantity used in the two-equation k-ω model is the specific dissipation rate (ω), which defines the rate at which turbulent eddies dissipate, and is defined as:

$$\omega = \frac{k^{1/2}}{C_\mu^{1/4} l} \tag{2}$$

with units [1/s], where l is the turbulence length scale and C_μ is an empirical model constant (typically set to 0.09 as default). Physically, the specific dissipation rate represents the rate at which turbulent energy (per unit mass) is converted to internal flow energy. The presence of turbulence in the flow field contributes to the diffusive behavior of the fluid with an effect similar to kinematic viscosity (v). To model this additional turbulence diffusion, the k and ω quantities are used to define a turbulent kinematic viscosity:

$$v_T = \frac{k}{\omega} \tag{3}$$

with units of (m^2/s).

In the dispersion parameters, flow and turbulence quantities are calculated as volume-averaged values within the region of the capsule and outlet capillary. With turbulence kinetic energy as an example, the volume-averaged quantities within the discretized computational domain are defined as:

$$k = \frac{1}{V_T} \sum_{i=1}^{n} k_i \times V_i \tag{4}$$

where V_T is the volume of the capsule and outlet capillary, k_i is the turbulent kinetic energy in Cell i, V_i is the volume of cell i, and the summation is across all cells in the capsule and outlet capillary region.

Evaluation of preliminary dispersion parameters began by identifying the correlation strength between experimental aerosolization metrics and the CFD-based parameters presented by Longest and Farkas (8), which were developed for low-volume devices (10 mL of actuation air) operated at higher pressures. In that study, the MMAD correlated well with k_{field}^* (ratio of volume-averaged k to inlet velocity squared) giving an R^2 value of 0.87, and with $k_{field}^* \times \omega_{field}^*$ (where ω_{field}^* is ω non-dimensionalized with a characteristic time scale) giving an R^2 value of 0.94. However, correlations of these dispersion parameters to MMAD for experimental iteration 1 devices in this study were not as strong, with R^2 values less than 0.6. Other dispersion parameters from the previous paper were also considered for MMAD correlation, but did not achieve an R^2 value greater than 0.8. For ED, the previous Longest and Farkas study (8) showed that k_{field}^* and $k_{field}^* \times \omega_{field}^*$ had a strong correlation with R^2 values of 0.96 and 0.98, respectively, again for different low-volume high-pressure devices. Though similar to MMAD in the present study, these dispersion parameters did not show the same correlation strength to ED with experimental iteration 1, with R^2 values again below 0.6. Therefore, new dispersion parameters were required that were developed specifically for this pediatric air-jet DPI and its operating conditions.

In parameter development for the pediatric air-jet DPI, approximately 40 dispersion parameters were correlated with both MMAD and ED. These dispersion parameters used various combinations of variables for flow quantities, turbulence characteristics, design parameters, and operating conditions. The strongest correlations ($R^2 > 0.8$) from this new batch of dispersion parameters for experimental iteration 1 were identified and the variables used in their development were tested for accuracy and robustness in experimental iteration 2. The strength of correlation for the new dispersion parameters developed in the present study are given in the "RESULTS" section. They are summarized here to discuss the variables from which they are constructed and how they aim to describe the device flow conditions.

For MMAD, the dispersion parameters that gave to the strongest correlation with experimental iterations 1 and 2 ($R^2 > 0.8$) are summarized in Table II. To improve correlation agreement with the MMAD experimental data, a common theme in all of the dispersion parameters was the inclusion of the actuation pressure, or ΔP, which represents the input flow energy per unit volume (J/m^3). The dispersion parameter that gave the strongest correlations with MMAD was:

$$\frac{kd^*}{\Delta P v_i} \tag{5}$$

where d^* is the ratio of outlet to inlet capillary diameters and v_i is the inlet capillary velocity. The physical basis for this dispersion parameter is the input turbulent kinetic energy (k in J/kg) per input flow energy (ΔP in J/m^3). Division by air density can be used to eliminate the differing basis of the energy terms, but it is not necessary considering that all cases are actuated with room air. Based on trial and error experimentation, the correlation with MMAD was significantly improved by multiplying the dispersion parameter by d^*/v_i, similar to the result of Longest and Farkas (8).

The $\Delta P/k^* d^*$ parameter in Table II is similar to Eq. (5), but the ratio of k to inlet velocity is non-dimensionalized as it was by Longest and Farkas (8). The numerators and denominators are also reversed as this gave a better R^2 value. The $k\mu/v_i\Delta P d_o$ parameter again includes similar variables as the previous two parameters, but uses inspiration from the Bejan number (39) (Be $= \Delta P L^2/\mu v$, which represents a non-dimensional pressure drop) to non-dimensionalize the parameter. The $k^* \omega^* d^*$ parameter applies the ratio of outlet to inlet diameter to the $k^* \times \omega^*$ parameter from Longest and Farkas (8), which had a positive influence on the R^2 value for all cases considered. Finally, the $v_i' d^*/v_i \Delta P$ parameter is again similar to the first dispersion parameter discussed here, but the ratio of k to inlet velocity is non-dimensionalized by using the fluctuating velocity component ($v' = \sqrt{2/3k}$) instead of k.

For ED, the dispersion parameters that gave the strongest correlation with experimental iterations 1 and 2 ($R^2 > 0.8$) are summarized in Table III. In contrast to Longest and Farkas (8), none of the dispersion parameters that utilize a combination of flow and turbulence quantities (such as v_i and k) had a strong correlation with ED in the current study, which evaluates a pediatric air-jet DPI as opposed to a low actuation volume DPI. All dispersion parameters for ED presented in this study use inlet volumetric flow rate (Q_i) with a scale factor as a prediction of aerosolization performance. The scale factors that were most effective were d^*, k, and d_o, which all improved the correlation from an R^2 value of 0.74 to over the threshold of 0.8 for a strong correlation in this study.

Evaluation and Comparison Criteria

This study uses the following metrics to quantify device performance improvements, compare the match between experimental and CFD results and determine the accuracy of dispersion parameter predictions.

The Relative Δ metric compares the predicted aerosolization performance of design configurations with experimental iteration 1, in order to quantify performance improvements over the initial designs. It is defined as the difference between the CFD-predicted MMAD (MMAD$_{CFD}$) and the estimated MMAD (MMAD$_{Est}$), based on the estimated MMAD from experimental iteration 1, relative to the estimated MMAD:

$$Relative\ \Delta = \frac{MMAD_{CFD} - MMAD_{Est}}{MMAD_{Est}} \times 100\% \tag{6}$$

Table II. Summary of Evaluated MMAD Correlation Parameters Ranked in Order of Preference Based on R^2 Value

Parameter	Units	Variables	Definitions
$\frac{kd^*}{\Delta P v_i}$	$\left[\frac{m}{Pa\text{-}s}\right]$	$d^* = \frac{d_o}{d_i}$	k: Turbulent kinetic energy
			d^*: Non-dimensional length scale
			v_i: Inlet capillary velocity
			ΔP: Pressure drop across device
$\frac{\Delta P}{k^* d^*}$	[Pa]	$k^* = \frac{k}{v_i^2}$	k^*: Non-dimensional k^{a}
$\frac{k\mu}{v_i \Delta P d_o}$	[−]		μ: Fluid velocity
$k^* \omega^* d^*$	[−]		ω^*: Non-dimensional ω^{a}
$\frac{v_i' d^*}{v_i \Delta P}$	$\left[\frac{1}{Pa}\right]$	$v_i' = \sqrt{2/3k}$	v': Fluctuating velocity due to turbulence

^{a} Non-dimensional turbulence parameters presented by Longest and Farkas (8)

Table III. Summary of Evaluated ED Correlation Parameters Ranked in Order of Preference Based on R^2 Value

Parameter	Units	Variables	Definitions
$Q_i d^*$	[LPM]	$d^* = \frac{d_o}{d_i}$	Q_i: Volumetric flow rate through the inlet capillary
$Q_i k$	$\left[\frac{m^5}{s^3}\right]$		k: Turbulent kinetic energy
$Q_i d_o$	$\left[\frac{m^4}{s}\right]$		d_o: Outlet capillary diameter

The R^2 value for correlation between emitted dose and Q_i alone is 0.74, hence scaling by d^*, k, or d_o improves the strength of correlation to $R^2 > 0.8$

Specifically, estimated MMAD ($MMAD_{Est}$) is determined from the experimental data by the linear line of best fit between MMAD and ED for experimental iteration 1, which is hereafter referred to as experimental iteration 1 best fit. That is, if a device configuration has a predicted MMAD and ED that lies on experimental iteration 1 best fit, its relative Δ is zero and there is no improvement over the initial devices. If the relative Δ is negative, its MMAD is smaller than would be predicted by ED alone, based on the results from experimental iteration 1 and *vice versa* for a positive relative Δ. Therefore, a negative relative Δ shows an improvement in aerosolization performance over experimental iteration 1 for a given ED.

Relative difference (Rel. Diff.) is a standard statistical measure but has different definitions given the application. In this instance, the difference is between the CFD-predicted and experimental (Exp) MMAD or ED, relative to the experimental value:

$$\text{Rel. Diff.} = \frac{MMAD_{\text{CFD}} - MMAD_{\text{Exp}}}{MMAD_{\text{Exp}}} \times 100 \; or \; \frac{ED_{\text{CFD}} - ED_{\text{Exp}}}{ED_{\text{Exp}}} \times 100 \tag{7}$$

This provides a basis for comparison between the CFD-predicted and experimentally determined aerosolization performance.

RMS error is also commonly used in statistical methods. It is the square-root of the sum-square of the difference between CFD-predicted and experimental results divided by the number of data points:

$$\text{RMS Error} = \sqrt{\frac{\sum_{i=1}^{n}\left(MMAD_{\text{CFD,i}} - MMAD_{\text{Exp,i}}\right)^2}{n}} \; or \tag{8}$$

$$\sqrt{\frac{\sum_{i=1}^{n}\left(ED_{\text{CFD,i}} - ED_{\text{Exp,i}}\right)^2}{n}}$$

This quantifies the error between the CFD-predicted and experimentally observed aerosolization performance across all cases considered by the study.

RESULTS

First and Second Experimental Iterations

Figure 3 plots the MMAD against ED for cases 1–4 from experimental iteration 1, and the dashed line is experimental iteration 1 best fit ($R^2 = 0.98$). The numerical annotations in the plot correspond to the markers for each device in Table IV. This plot shows that for these cases, increasing ED also increases MMAD. This is undesirable for DPI aerosolization performance, as we want both a small MMAD and large ED to deliver as much drug to the target area of the lungs as possible. Therefore, for improvement in aerosolization performance we intend to develop devices that perform below this dashed line. That is, for a given ED, the MMAD should be smaller than estimated from the linear fit performance of experimental iteration 1.

Experimental iteration 2 intended to test the accuracy and robustness of initial dispersion parameter development, identify additional dispersion parameters, and evaluate what aspects of device design and operation would plot MMAD and ED above or below the experimental iteration 1 best fit. Figure 4 adds the MMAD and ED data from experimental iteration 2 (Table IV) to Fig. 3. The numeral annotations in the plot correspond to the markers for each device in Table IV. From this figure, it is clear that the majority of cases exhibited similar or worse performance than experimental iteration 1, as they plot close to or above the dashed line. The exception is case 3.00/2.08 (VI), which has an MMAD that is approximately 0.5 μm smaller than what is expected from its ED and performance estimations from experimental iteration 1.

The experimental results from experimental iterations 1 and 2, with CFD predictions of the flow and turbulence fields for each device, were used to develop the dispersion parameters for MMAD and ED that were summarized by Tables II and III, respectively. The strength of MMAD and ED correlations that use these parameters is presented in subsequent sections. In line with the study objective, CFD-predictions of aerosolization performance use the dispersion parameters, and their associated correlations, to drive optimization of the device design.

Flow and Turbulence Characteristics

Before presenting details on the dispersion parameters, aerosolization performance, and device optimization, it is important to understand the flow field behavior and characteristics within the device. As mentioned in the "MATERIALS AND METHODS" section, the flow is highly turbulent and moderately compressible, with inlet Reynolds numbers over 10,000 and Mach numbers up to 0.27 for the cases in experimental iterations 1 and 2. Figure 5 shows contours of k and velocity streamlines within the capsule of case 4. The highest level of turbulence, represented with k, occurs in the shear layer where the inlet jet meets the relatively quiescent flow in the capsule, which propagates through the outlet capillary. There is also a large velocity gradient between the center of the inlet jet and the dose chamber. Points A (center of the jet) and B (top of powder bed) in Fig. 5 have velocity magnitudes of 110.36 and 4.39 m/s respectively (or Mach numbers of 0.32 and 0.01) with only 1.88 mm between them. The velocity streamlines in Fig. 5 demonstrate very dynamic and chaotic behavior in the secondary flow patterns within the capsule.

As mentioned previously, preliminary experimental work tested whether angled inlets or a longer outlet capillary would improve aerosolization performance with increased secondary flow or more exposure to highly turbulent flow, respectively. It is reasonable to expect that increased secondary flow patterns would entrain more particles from the powder bed and provide an improvement in ED. However, the preliminary work showed little aerosolization improvement for devices with an inlet capillary angled at 30°, 60°, and 90° relative to the long axis of the capsule. CFD predictions of secondary flow, with the stream-wise flow considered to be aligned with long axis, also did not correlate well with ED. It is also reasonable to expect that exposing particle
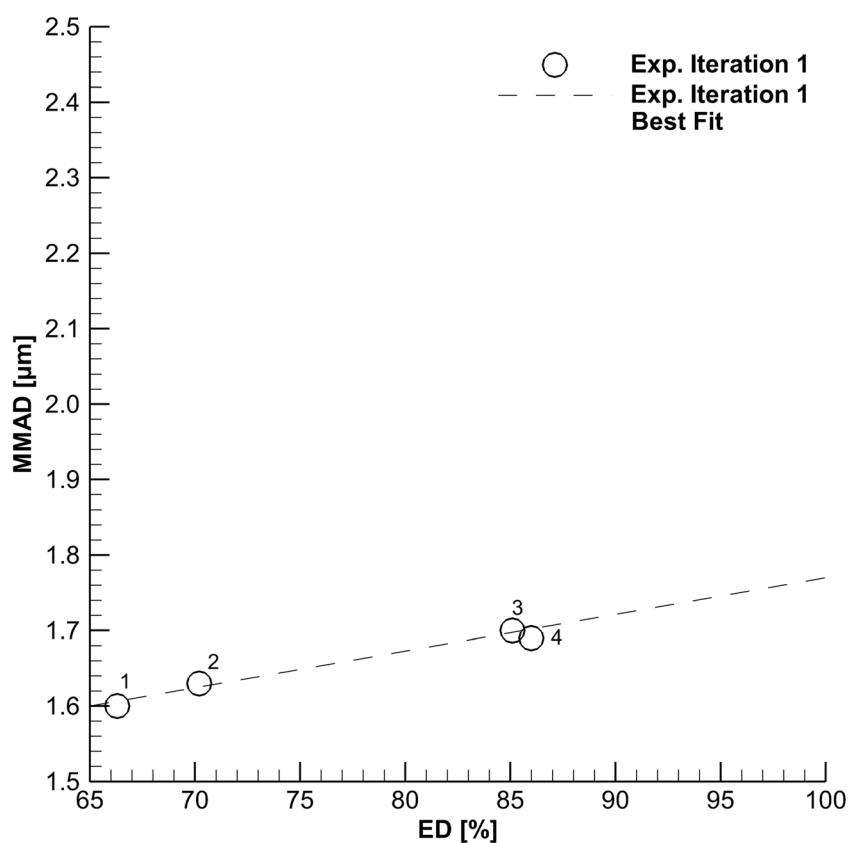
Fig. 3. Plot of particle mass-median aerodynamic diameter (MMAD) against emitted dose (ED) for experimental iteration 1 (cases 1–4). Annotations correspond with the markers in Table IV. A small MMAD and large ED is desirable for aerosolization performance. The dashed line is experimental iteration 1 best fit ($R^2 = 0.98$), where particle size generally worsens with an improvement in emitted dose

agglomerates to highly turbulent flow for a longer duration would aid secondary breakup and reduce MMAD. However, extending the length of the outlet capillary from 18 to 30 mm and 60 mm also showed negligible improvement in aerosolization performance.

Table IV. Summary of Aerosolization Performance for Experimental Iterations 1 and 2. Experimental Values Are Given as Means with Standard Deviations Shown in Parenthesis ($n = 3$)

Name	d_i (mm)	d_o (mm)	MMAD (μm)	ED (%)	Marker
Experimental iteration 1					
Case 1[a]	1.52	1.52	1.60 (0.16)	66.3 (3.1)	1
Case 2[a]	1.40	1.80	1.63 (0.06)	70.2 (1.7)	2
Case 3[a]	2.39	2.39	1.70 (0.18)	85.1 (8.8)	3
Case 4[a]	1.83	2.39	1.69 (0.01)	86.0 (1.4)	4
Experimental iteration 2					
Half Q	1.83	2.39	2.46 (0.21)	72.0 (5.6)	I
1.32/2.39	1.32	2.39	1.85 (0.10)	77.9 (1.8)	II
1.60/2.39	1.60	2.39	1.71 (0.03)	83.5 (1.5)	III
2.08/2.69	2.08	2.69	1.84 (0.09)	88.7 (1.2)	IV
1.32/2.90	1.32	2.90	2.11 (0.09)	73.3 (1.2)	V
3.00/2.08	3.00	2.08	1.61 (0.08)	80.7 (5.9)	VI

[a] Results presented by Farkas *et al.* (21)

This raises questions over the mechanisms within the device that are responsible for the most effective forms of powder aerosolization. The large velocity gradient between the inlet jet and remainder of the capsule region creates the correct amount of secondary flow in order to maintain a high ED and not fluidize the powder bed too quickly. Also, the maximum k to which particle agglomerates are exposed may drive secondary breakup and determine particle size, as opposed to time of exposure. That is, if agglomerates pass through the region of highest energy eddies and break up as small as that energy permits, additional exposure time to smaller energy eddies may not reduce the particle size further. This observation would explain why a longer outlet capillary length did not further reduce MMAD.

Particle Size and Emitted Dose Dispersion Parameters

Figure 6 plots MMAD as a function of the dispersion parameter from Table II with the strongest correlation. For the $kd^*/v_i\Delta P$ dispersion parameter, the R^2 value is 0.96 and standard error (SE) is 0.06 μm when correlated with MMAD. The dashed line on the plot is the linear line of best fit between cases considered and represents the correlation used to predict MMAD from the dispersion parameter. Considering the 95% interval on a normal distribution, we can assume
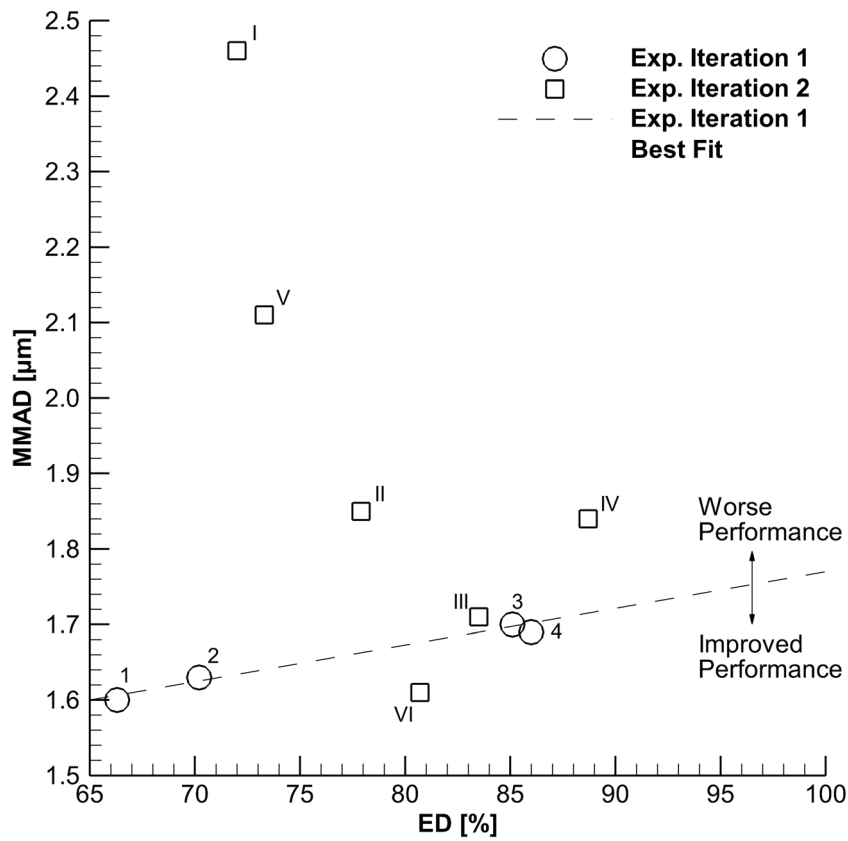
Fig. 4. Addition of experimental iteration 2 to the MMAD vs. ED plot shown in Fig. 3. Annotations correspond with the markers in Table IV. Generally, these additional devices perform poorly compared to cases 1–4, except case 3.00/2.08 (VI), which has better MMAD for a given ED

the correlation is accurate between plus or minus double the SE, which is 0.12 μm and represented by the solid lines on Fig. 6. For context, the coefficient of variation (CoV) is defined as the ratio of SE to the mean MMAD, which in this case is 3.3%.

The high R^2 value, small SE, and small CoV demonstrates a very strong correlation between MMAD and the $kd^*/v_i\Delta P$ dispersion parameter. Beyond the statistical measures, the plot of data points for each case relative to the linear correlation line also suggests the $kd^*/v_i\Delta P$ dispersion parameter will accurately predict MMAD

from CFD results. The correlation closely matches the full range of data points, from devices with a relatively small (1.6 μm) to larger (2.4 μm) MMAD, and also captures the effect of operating case 4 with a lower pressure drop with the half Q case. Furthermore, the correlation provides an accurate prediction for case 1.32/2.90, with its MMAD in the middle ground between the 1.6–1.8 μm cases and the 2.4 μm half Q case, which further demonstrates the correlation is accurate across a range of dispersion parameters and MMAD values. Finally, CFD results for case 1.32/2.39 and 2.08/2.69 both show these devices had very
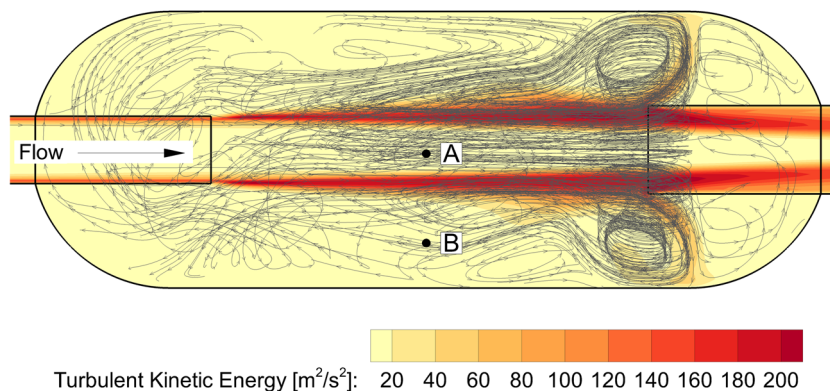

Fig. 5. Overlay plot on the mid-plane slice of turbulent kinetic energy field and flow streamlines between the inlet and outlet capillaries in the capsule. Velocity magnitudes at points A and B are 110.36 m/s and 4.39 m/s, respectively
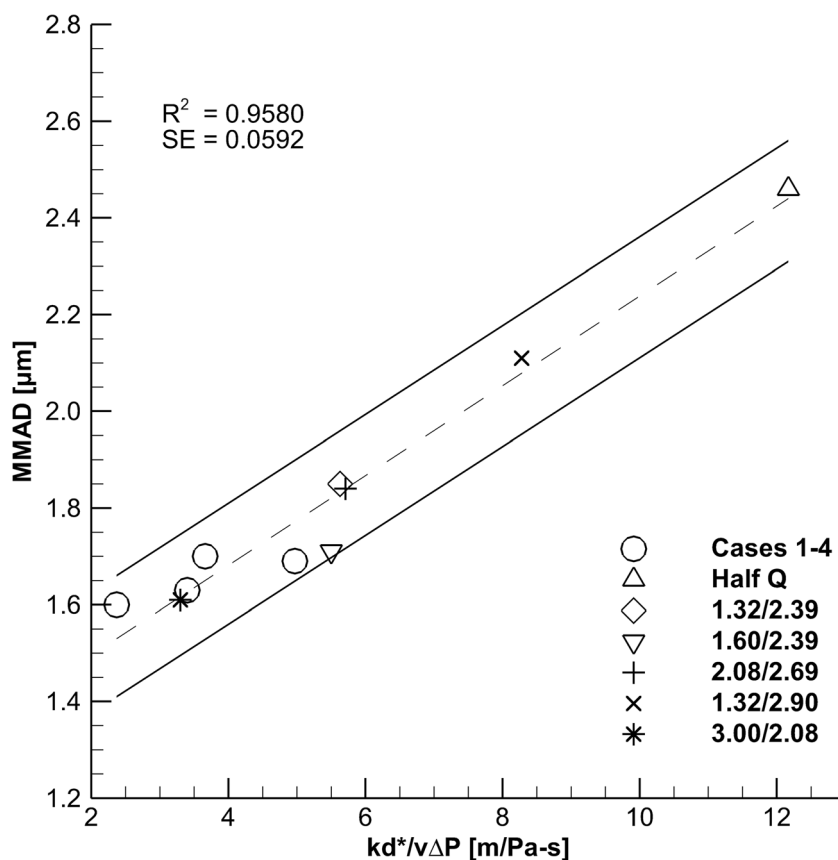
Fig. 6. Particle mass-median aerodynamic diameter (MMAD) vs. dispersion parameter $kd^*/v_i \Delta P$. The dashed line is the linear best fit and the solid lines show ± 0.12 μm, which is double the standard error (or the 95% interval on a normal distribution). Note that the half Q (triangle), 1.32/2.39 (diamond), 1.60/2.39 (inverted triangle), 2.08/2.69 (plus sign), 1.32/2.90 (cross), and 3.00/2.08 (asterisk) cases are from experimental iteration 2 (squares in Fig. 4)

similar dispersion parameter values, and the correlation is able to accurately predict they have the same MMAD. That is, if these cases had the same dispersion parameter value, but very different experimentally determined MMADs, the correlation would clearly be inaccurate.

Similar to the MMAD dispersion parameters, Fig. 7 plots ED as a function of the dispersion parameter from Table III with the strongest correlation. As before, the dashed line is the linear correlation (or line of best fit) and the solid lines represent plus or minus double the SE (or the 95% interval on a normal distribution). For the Qd^* dispersion parameter, the R^2 value is 0.86, the SE is 3.0%, and CoV is 3.8% when correlated with ED. As mentioned previously, out of all the dispersion parameters considered, the device ED consistently showed the best correlations with parameters that used the flow rate (Q) through the device. Correlating ED with Q alone showed an R^2 value of 0.74, and scaling by the variables summarized in Table III improved the correlations.

Influence of Design Factors on Dispersion

To be predictive of device aerosolization performance, it is necessary to understand how the CFD-predicted flow and turbulence variables in the MMAD and ED dispersion parameters behave in response to design factor changes.

These variables are volume-averaged turbulent kinetic energy (k) and inlet capillary velocity (v_i) in the MMAD dispersion parameter, and inlet volumetric flow rate (Q_i) in the ED dispersion parameter, with v_i directly calculated from Q_i. Figure 8 is a 3D surface plot of the CFD-predicted k vs. inlet and outlet capillary diameters on the independent axes; and Figure 9 shows CFD-predicted Q vs. inlet and outlet capillary diameters. These data points are the result of running an array of 144 CFD models for every possible combination of 12 different inlet and outlet capillary diameters ranging from 0.41 to 3.00 mm. An effort was made to combine the inlet and outlet diameters into a single function that could describe the device behavior, with respect to the dispersion parameter variables, in a standard x-y plot. However, the clearest representation of how the flow and turbulence quantities vary in response to design factor changes is with a 3D surface plot, as both k and Q_i are dependent on d_i and d_o by different relations. To estimate variable values in between the CFD-predicted data points, one could define a high-order bivariate polynomial to establish a surface of best fit. However, in this case, the large number of CFD simulations was sufficient to identify design factor configurations that were possible candidates for an optimized device.

Considering both Figs. 8 and 9 together, there is a region where d_i and d_o are greater than 2.5 mm that shows k
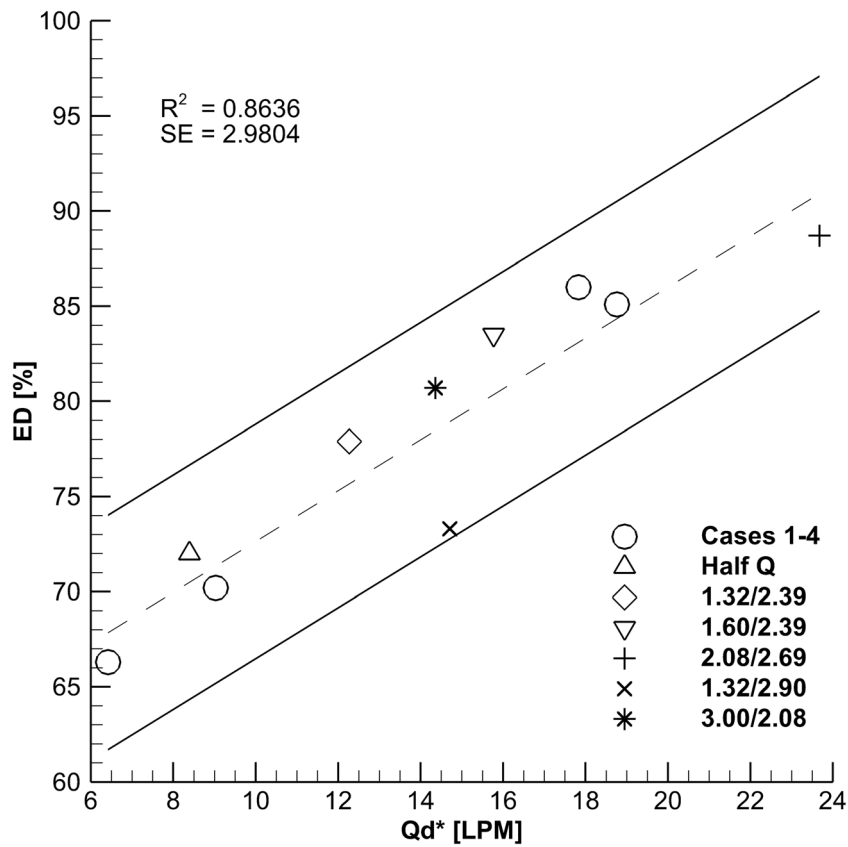
Fig. 7. Emitted dose (ED) vs. dispersion parameter $Qd*$. The dashed line is the linear best fit and the solid lines show $\pm 6.17\%$, which is double the standard error (or the 95% interval on a normal distribution). Note that the half Q (triangle), 1.32/2.39 (diamond), 1.60/2.39 (inverted triangle), 2.08/2.69 (plus sign), 1.32/2.90 (cross), and 3.00/2.08 (asterisk) cases are from experimental iteration 2 (squares in Fig. 4)
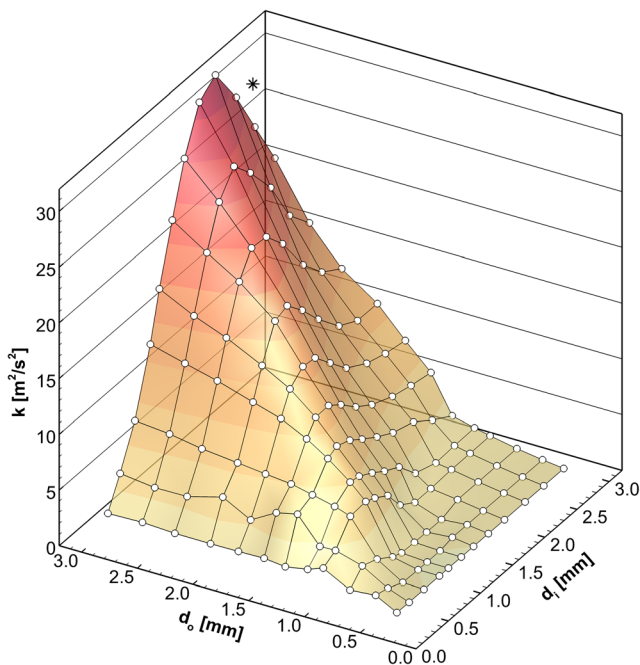

Fig. 8. 3D plot of CFD-predicted data points for turbulent kinetic energy (k) vs. inlet and outlet capillary diameter (d_i and d_o, respectively). The MMAD dispersion parameter (shown in Fig. 6) suggests smaller particles sizes are produced when k is small and inlet velocity (v_i) is high
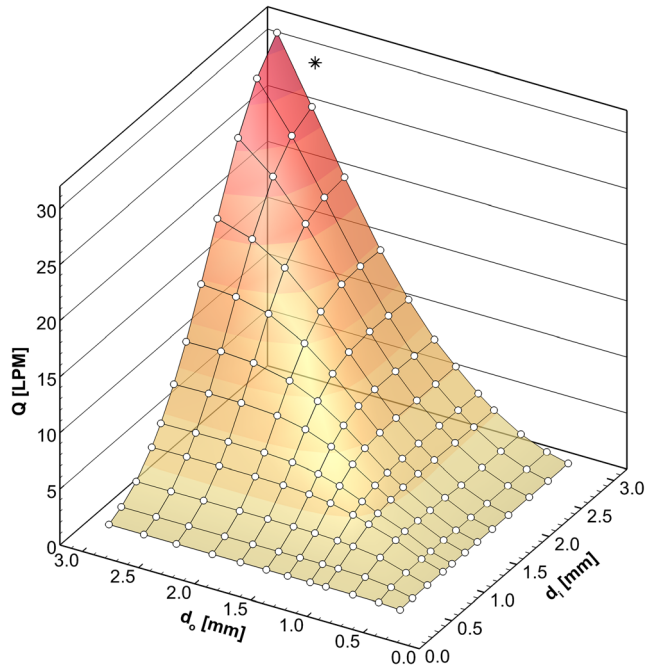
Fig. 9. 3D plot of CFD-predicted data points for flow rate (Q) vs. inlet and outlet capillary diameter (d_i and d_o, respectively). The ED dispersion parameter (shown in Fig. 7) suggests that emitted dose is improved when the flow rate is increased, but there is a limit given the administration of the devices to children

Table V. Summary of Cases with Inlet and Outlet Diameters Greater than 1.83 mm, Which Are in the Range of Design Configurations That Are Similar to Case 4. Cases Shown Are a Subset of a Full Array of 144 CFD Runs (All Possible Configurations of 12 different Capillary Sizes)

d_i (mm)	d_o (mm)	CFD MMAD (μm)	CFD ED (%)	Marker
1.83	1.83	1.58	72.8	AA
	2.08	1.65	77.6	AB
	2.39	1.77	83.4	4[a]
	2.69	1.92	87.7	AD
	3.00	2.10	91.5	AE
2.08	1.83	1.55	71.9	BA
	2.08	1.61	77.5	BB
	2.39	1.71	84.9	BC
	2.69	1.82	91.0	BD
	3.00	2.03	96.5	BE
2.39	1.83	1.55	70.5	CA
	2.08	1.58	76.1	CB
	2.39	1.64	84.6	3[b]
	2.69	1.75	92.7	CD
	3.00	1.88	100.0[d]	CE
2.69	1.83	1.56	69.2	DA
	2.08	1.59	74.4	DB
	2.39	1.62	82.9	**DC**
	2.69	1.68	92.0	**DD**[c]
	3.00	1.79	100.0[d]	DE
3.00	1.83	1.58	68.1	EA
	2.08	1.62	72.7	EB
	2.39	1.63	80.8	**EC**
	2.69	1.66	89.9	**ED**[c]
	3.00	1.72	100.0[d]	**EE**

Markers in bold have CFD-predicted MMAD and ED that plot below experimental iteration 1 best fit

[a] Same inlet and outlet configuration as case 4
[b] Same inlet and outlet configuration as case 3
[c] Candidate configurations selected for optimized design experimental evaluation
[d] Cases where the correlations predicted greater than 100% ED were capped at 100%

decreases (reducing MMAD) while Q continues to increase (improving ED). This region of high Q and decreasing k is labeled with ✷ in Figs. 8 and 9. Combining this with the MMAD and ED dispersion parameters ($kd^*/\Delta Pv_i$ and $Q_i d^*$ respectively), Figs. 8 and 9 suggest that device configurations in this region would give a small MMAD and high ED, which is the desirable aerosolization performance. For a constant ΔP and d^*, reducing k and increasing v_i would give a smaller MMAD dispersion parameter and predicts a smaller particle size. Likewise, for a constant d^*, increasing Q_i would give a larger ED dispersion parameter and predict less device losses. However, the predicted aerosolization performance from design factors is not quite as simple as what has been described here, as changing the inlet and outlet capillary diameters also changes the d^* variable, which has an effect on both the MMAD and ED dispersion parameters. Furthermore, the Q through the devices in the region where d_i and d_o is greater than 2.5 mm is over 20 LPM, which for an inhalation volume of 750 mL gives an actuation time of less

than 2 s. Therefore, the Q for these devices might be too high for the target age of a 5–6-year-old subject. That said, it is valuable insight for developing devices that may target older patients that inhale at higher flow rates. One final consideration regarding actuating DPIs with higher flow rates is the resultant impaction parameter (typically given as $d_a^2 Q$, where d_a is aerodynamic particle diameter) may be higher, which would suggest the possibility of increased extrathoracic losses (40–43).

Aerosolization Performance and Device Optimization

As described above, possible device design configurations from 12 inlet and outlet capillary diameters were considered, ranging from 0.41 to 3.00 mm, which required the evaluation of 144 CFD models. The majority of these models, especially those with relatively small capillary diameters, showed little improvement over case 4, which has exhibited the best aerosolization performance from experimental iterations 1 and 2. Table V summarizes the CFD-predicted aerosolization performance, from flow and turbulence quantities and dispersion parameter correlations, of 25 cases that had inlet and outlet diameters greater than 1.83 mm (as this is the inlet capillary diameter for case 4). The naming convention for the markers, which are used in subsequent plots to identify each case, uses the first letter to identify the inlet capillary diameter and the second letter for the outlet, where A is 1.83 mm, B is 2.08 mm, C is 2.39 mm, D is 2.69 mm, and E is 3.00 mm. The cases with markers highlighted in bold are those where CFD-based predictions suggest that both the MMAD and ED will be better than the aerosolization performance of case 4. Here, better means the CFD-predicted MMAD and ED plot below experimental iteration 1 best fit. What is most interesting from this data set is the CFD-based predictions show that ED can increase as MMAD decreases (as Figs. 8 and 9 suggested), which was not apparent from experimental iteration 1. For example, for cases AD and CD, the inlet diameter changes from 1.83 to 2.39 mm and outlet diameter is constant at 2.69 mm, with the CFD-predicted MMAD improving from 1.92 to 1.75 μm and ED improving from 87.7 to 92.7%. Conversely, in experimental iteration 1, cases 3 and 4 had the same outlet diameter, but inlet diameters of 2.39 mm and 1.83 mm, respectively, and they showed little difference in aerosolization, with case 4 having a marginally better ED.

Figure 10 adds the MMAD and ED data for the cases that CFD-based predictions suggest are better than case 4 (i.e., the bold cases in Table V) to Fig. 4. The additional annotations in the plot correspond to the markers for each case in Table V. As mentioned previously, cases that plot below the dashed line exhibit an improvement in aerosolization performance compared to experimental iteration 1. The "Evaluation and Comparison Criteria" section defined the relative Δ metric that compares the estimated MMAD (for a given ED) with the performance of devices from experimental iteration 1. This provides a quantitative value to measure the difference between the CFD-based predictions and the dashed line in Fig. 10. Table VI summarizes the relative Δ metric for each of the cases added to Fig. 10, with a negative value indicating the performance is an improvement over experimental iteration 1 and the value quantifying the
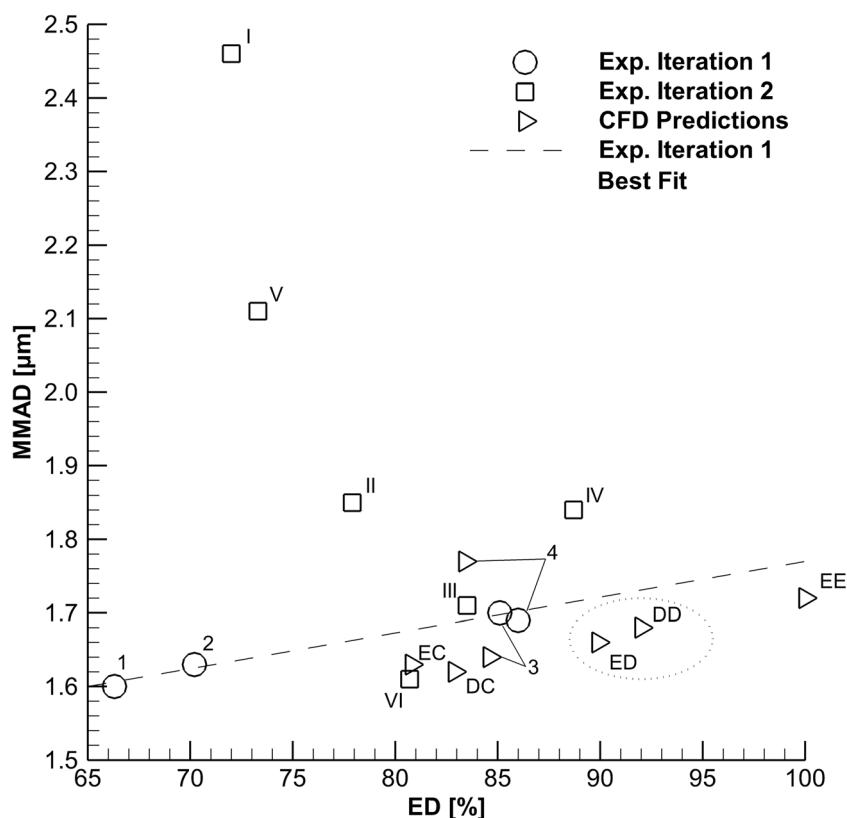
Fig. 10. Addition of CFD-predicted aerosolization performance to the MMAD vs. ED plot shown in Fig. 4. Annotations correspond with the markers in Tables IV and VI. The devices annotated with ED and DD are selected as the optimized devices as they have an ED prediction greater than 90%, better predicted MMAD than case 4, and show improved device performance compared to experimental iteration 1

percentage improvement in aerosolization performance. From all the design configurations considered here, cases 2.69/2.69 and 3.00/2.69 (DD and ED) are selected for device optimization evaluation as they are predicted to have a smaller MMAD than case 4, a negative relative Δ, and an ED greater than 90%. These two cases are highlighted with the dotted ellipse in Fig. 10.

Figure 10 also provides a comparison between the CFD-based predictions and experimentally measured MMAD and ED for cases 3 and 4. These data points lie within the SE of the MMAD and ED correlation and the standard deviation (SD) of the experimental data. The accuracy of CFD-based

predictions, with statistical observations, is discussed in greater detail in the following section.

Experimental Validation

Table VII summarizes the comparison between CFD-based predictions and experimentally measured MMAD and ED for all experimentally tested devices. The comparison to experimental iterations 1 and 2 serves as the typical validation of CFD methods and the dispersion parameter correlations with experimental data. The comparison with the two optimized devices provides an *a priori* validation of the

Table VI. Summary of CFD-Predicted ED and MMAD Compared to the Estimated MMAD Based on Experimental Iteration 1 Best Fit. Cases Shown Are Those That the CFD Predicts Will Perform Better than Case 4 Based on the Data in Table V

d_i (mm)	d_o (mm)	CFD ED (%)	CFD MMAD (μm)	Estimated MMAD (μm)	Relative Δ (%)	Markers
2.69	2.39	82.9	1.62	1.68	− 3.89	DC
	2.69	92.0	1.68	1.73	− 2.72[a]	DD
3.00	2.39	80.8	1.63	1.67	− 2.65	EC
	2.69	89.9	1.66	1.72	− 3.36[a]	ED
	3.00	100.0	1.72	1.76	− 2.51	EE

Relative Δ is the relative difference between the CFD-predicted MMAD and the estimated MMAD based on experimental iteration 1 best fit
[a] Candidate configurations selected for optimized design experimental evaluation

Table VII. Summary of Relative Difference (Rel. Diff.) Between the CFD-Predicted (CFD) and Experimental (Exp.) MMAD and ED. The Data Shows How Accurately the CFD and Dispersion Parameter Correlations Predicted Experimental Aerosolization Performance. Experimental Values Are Given as Means with Standard Deviations Shown in Parenthesis ($n = 3$)

Name	d_i (mm)	d_o (mm)	MMAD			ED			Marker
			CFD (μm)	Exp. (μm)	Rel. Diff. (%)	CFD (%)	Exp. (%)	Rel. Diff. (%)	
Experimental iteration 1									
Case 1	1.52	1.52	1.53	1.60 (0.16)	4.2	67.9	66.3 (3.1)	2.3	1
Case 2	1.40	1.80	1.63	1.63 (0.06)	0.2	71.3	70.2 (1.7)	1.6	2
Case 3	2.39	2.39	1.65	1.70 (0.18)	2.9	84.3	85.1 (8.8)	0.9	3
Case 4	1.83	2.39	1.77	1.69 (0.01)	4.8	83.1	86.0 (1.4)	3.4	4
Experimental iteration 2									
Half Q	1.83	2.39	2.44	2.46 (0.21)	1.0	70.5	72.0 (5.6)	2.1	I
1.32/2.39	1.32	2.39	1.83	1.85 (0.10)	0.9	75.7	77.9 (1.8)	2.9	II
1.60/2.39	1.60	2.39	1.82	1.71 (0.03)	6.5	80.3	83.5 (1.5)	3.8	III
2.08/2.69	2.08	2.69	1.84	1.84 (0.09)	0.0	90.9	88.7 (1.2)	2.5	IV
1.32/2.90	1.32	2.90	2.08	2.11 (0.09)	1.6	78.9	73.3 (1.2)	7.7	V
3.00/2.08	3.00	2.08	1.62	1.61 (0.08)	0.5	72.8	80.7 (5.9)	9.8	VI
Optimized devices									
2.69/2.69	2.69	2.69	1.68	1.55 (0.13)	8.4	92.0	90.4 (2.8)	1.8	DD
3.00/2.69	3.00	2.69	1.66	1.59 (0.05)	4.4	89.9	92.3 (0.2)	2.6	ED

optimization process. That is, the CFD-based predictions of the MMAD and ED for those two design configurations were established before validating their accuracy with experimental testing, and no adjustments to either the CFD models or dispersion parameter correlations were made after obtaining the experimental data. The Rel. Diff. in Table VII uses the standard definition for observed and predicted data. The average Rel. Diff. between CFD-based predictions and experimental measurements for MMAD is 2.9%, and the range of absolute error is from -0.07 to 0.13 μm (case 1 and case 2.69/2.69, respectively). Similarly, for ED the average Rel. Diff. is 3.5% and the range of absolute error is from -7.9 to 5.6% (case 3.00/2.08 and 1.32/2.90, respectively). The RMS error for MMAD and ED is 0.06 μm and 3.4%, respectively, which compares well with the SE from each of the MMAD and ED dispersion parameter correlations. Based on these statistical measures, the CFD flow and turbulence fields with $kd^*/\Delta Pv_i$ and Qd^* dispersion parameters provide a very good prediction of device aerosolization performance, verified with *a priori* validation.

Finally, the design configurations that were selected as candidates for optimized devices provided improved aerosolization performance compared to case 4. The MMAD decreased from 1.69 to 1.55 μm and 1.59 μm, which is an absolute difference of 0.14 μm and 0.10 μm, for cases 2.69/2.69 and 2.69/3.00, respectively. Similarly, the ED increased from 86.0 to 90.4% and 92.3%, which is an absolute difference of 4.4% and 6.3%. This device optimization would not be possible without the insight into the relationship between aerosolization performance and design factors that was possible with a concurrent CFD and experimental approach.

DISCUSSION

This study meets the objective by establishing dispersion parameter correlations ($kd^*/\Delta Pv_i$ and Qd^*) that accurately predict the aerosolization performance (MMAD and ED) of a pediatric air-jet DPI. Using these dispersion parameters, a full sweep of 144 CFD models, covering every configuration of 12 different inlet and outlet diameter capillaries, was evaluated for optimized predicted performance. Two candidate optimized design configurations were validated *a priori*, and found to have improved aerosolization performance compared to case 4. Throughout the study, valuable insights into the flow and turbulence conditions within the capsule were obtained, and relationships between CFD flow and turbulence fields and design factors were established.

The flow within the capsule during actuation of the DPI is surprisingly complex given the relatively simple geometry. Inlet Mach and Reynolds numbers suggest moderately compressible and highly turbulent flow, especially for cases with larger capillary diameters and high flow rates, and high frequency flow oscillations require a transient solution strategy. Analysis of the CFD velocity field shows a large velocity gradient between the center of the inlet jet and quiescent capsule (from 110.4 to 4.4 m/s across a distance of 1.88 mm). The velocity gradient has an equally large negative pressure gradient that generates the correct amount of secondary flow to aerosolize the powder bed at an adequate rate. This premise is supported by the fact that ED correlated well with device flow rate, meaning higher flow and velocities through the device lead to greater entrainment of particles from the powder bed. Furthermore, experimental iteration 1 showed that MMAD increased with ED, which suggests that a larger negative pressure gradient is capable of lifting the larger particles from the powder bed, hence the simultaneous increase in both aerosolization performance metrics for experimental iteration 1.

Beyond meeting the primary objective, this study also demonstrated how the flow and turbulence fields, which are used in the definition of the dispersion parameters, behave in response to changes in design factors. 3D surface plots show

that k and Q vary relative to inlet and outlet capillary diameters as independent variables. Results showed that capillary diameters larger than approximately 2.5 mm lead to a relative decrease in k and increase in Q, which according to the dispersion parameters gives the desired decrease in MMAD and increase in ED. However, given the administration of the air-jet DPI to children, there is a relatively low upper limit on the available flow rate through the device to maintain low extrathoracic depositional losses, with the target being approximately 15 LPM for a 5–6-year-old subject.

The dispersion parameter correlations established in previous work by our group (8,9) did not correlate well with experimental iteration 1 in the present study and were further weakened when applied to experimental iteration 2. This is because of differences in the device and operation, including a larger air volume, higher flow rates, and larger capillary sizes in the current study. As such, new dispersion parameters were established that gave strong correlations, for both MMAD and ED, when applied to the current data set of ten experimental runs (see Table IV). What is consistent between the dispersion parameters used in the present study and previous work is that the MMAD is at least partially dependent on the ratio between volume-averaged k and inlet flow velocity. As k is specific turbulence kinetic energy and velocity is akin to specific flow kinetic energy, this ratio can be thought of as the ratio of turbulence to flow energy. That is, when aiming for a small particle size, one should strive to minimize this ratio and not necessarily minimize k alone. The addition of pressure drop across the device to the MMAD dispersion parameter accounts for the energy used to actuate the air-jet DPI.

This study also demonstrated the strength of the CFD methods and dispersion parameters used in predictions of aerosolization performance with *a priori* validation. Typically, CFD models are validated against experimental data after the devices have been tested, and the CFD model parameters are adjusted until numerical and experimental results match. In *a priori* validation, the devices are tested after the CFD models are run, and results between the numerical and experimental data are compared and reported with no changes to the CFD model setup. The results showed that the CFD models and aerosolization performance predictions for the two optimized devices were very close to the experimentally tested MMAD and ED, with small relative, absolute, and RMS errors. This demonstrates that the CFD methods for air-jet DPIs established by our previous work (8,9) and the newly defined dispersion parameters are accurate predictors of device performance.

The two candidate optimized designs decreased the experimentally measured MMAD by 0.10 to 0.14 μm (relative difference of 5.9 to 8.3%) and increased ED by 4.4 and 6.3% (relative difference of 5.1 to 7.4%) compared to case 4. Therefore, these two devices demonstrated improved aerosolization performance compared to previous air-jet DPI designs. However, there is more to consider when administering pharmaceutical aerosols to children with air-jet DPIs than only the device aerosolization performance. As mentioned previously, the flow rate through the optimized devices is approximately 25 LPM,

which, for a 750 mL inhalation volume, gives an actuation time of less than 2 s. For the target age of a 5–6-year-old child, the inhalation flow rate should be about 15 LPM and an actuation time of 3 s, meaning the optimized devices may increase extrathoracic losses for the age of patients selected as the focus of this study. That said, these devices may be suitable for older children with slightly larger extrathoracic airways. The impaction parameter ($d_a^2 Q$) is often used when evaluating extrathoracic aerosol deposition (40–43). There is a large amount of inter-patient variability when using this parameter, but the general trend is that particle deposition in the nasal (or oral) passage typically increases as the impaction parameter increases. This parameter shows that if the particle size (d_a) decreases, the extrathoracic losses may be the same or even increase if the flow rate (Q) increases. Comparing cases 2.69/2.69 and 3.00/2.69 to case 4, the impaction parameter increases to 59.6 μm²-LPM and 68.3 μm²-LPM from 38.0 μm²-LPM, which indicates extrathoracic losses will be higher for the optimized devices. However, the deposition *vs.* impaction parameter plots vary considerably for different age groups (and even from patient to patient within age groups) and typically have a non-linear S-shape profile, so the actual increase in extrathoracic losses may be negligible for the optimized devices.

On the experimental side, limitations in the present study are consistent with those reported by Farkas *et al.* (21). One additional limitation is the variability in actuating the device with a ventilation bag, which is the intended actuation method. Experiments used compressed air and a solenoid valve to actuate the devices with a pressure drop of 6 kPa. This provided consistency from device to device and provided a clear definition of boundary conditions for CFD models. However, variability in the operation of a ventilation bag to actuate the device between caregivers could influence aerosolization performance. Results from the half Q case showed that actuating case 4 with a pressure drop of 1.5 kPa gave an MMAD of 2.46 μm and ED of 72.0%, which was much worse than actuating case 4 with 6 kPa. This is perhaps at the extreme end of a low pressure drop, but demonstrates the variability in device performance relative to actuation pressure. As such, this should be taken into consideration when establishing caregiver operation guidelines for actuation of the device.

Another limitation is the large number of design options that are available for the air-jet DPI approach. Despite the large number of inlet and outlet capillary configurations that were considered, many of the design factors available for air-jet DPIs have not been evaluated. Preliminary work showed that angled inlet capillaries relative to the outlet and longer outlet capillaries did not improve aerosolization performance. However, many more aspects of the device design can be explored such as different size and shape aerosolization chambers (instead of a size 0 capsule), capillary piercing locations and orientation (instead of along the long axis of the capsule), and actuating the device with several smaller volumes of air (instead of 750 mL in one actuation). The negative pressure gradient between the inlet jet and powder bed and its effect on secondary velocities within the capsule

has been discussed previously. Changing the aerosolization chamber (or capsule) shape and size could leverage this phenomena to improve ED and would also need to be considered when loading the device with larger or smaller drug masses.

Future work on improving the aerosolization performance of air-jet DPIs should focus on expanding the exploration of the many available design factors and their influence on MMAD and ED. Future iterations of air-jet DPIs design can use the physical insight and dispersion parameters identified in the present study to drive the design and optimize performance further. It would also be interesting to test how robust the newly defined MMAD and ED dispersion parameters are when applied to the changes in design that were discussed here. The secondary breakup mechanism that reduces the particle size, after they are entrained in the flow, is also little understood at this stage. The MMAD dispersion parameter shows that the ratio of k to inlet velocity should be minimized to reduce particle size, but the exact characteristics of the flow and turbulence field that are responsible for secondary breakup are unclear. High-resolution, high-speed imaging of the particles within the device may provide some experimental insight into particle break up within the flow. Similarly, utilizing discrete element method (DEM) in numerical models could provide CFD insight into break up mechanisms for air-jet DPIs, but such a model would be difficult to validate and very computationally expensive.

CONCLUSION

In conclusion, newly developed dispersion parameters with CFD predictions of flow and turbulence quantities were capable of accurately predicting air-jet DPI aerosol performance in terms of MMAD and ED with *a priori* validation. Greater insight into the flow and turbulence characteristics within the capsule was obtained, and the effect of design factors on these quantities was identified. Optimized devices reduced the MMAD by approximately 0.1 μm and increased ED by approximately 5%. However, these devices may be better suited to children older than 5–6 years old due to increased device flow rates.

ACKNOWLEDGEMENTS

FUNDING INFORMATION

COMPLIANCE WITH ETHICAL STANDARDS

REFERENCES

1. Coates MS, Fletcher DF, Chan H-K, Raper JA. Effect of design on the performance of a dry powder inhaler using computational fluid dynamics. Part 1: grid structure and mouthpiece length. J Pharm Sci. 2004;93(11):2863–76.
2. Coates MS, Fletcher DF, Chan H-K, Raper JA. The role of capsule on the performance of a dry powder inhaler using computational and experimental analyses. Pharm Res. 2005;22(6):923–32.
3. Coates MS, Chan H-K, Fletcher DF, Raper JA. Influence of air flow on the performance of a dry powder inhaler using computational and experimental analyses. Pharm Res. 2005;22(9):1445–53.
4. Coates MS, Chan H-K, Fletcher DF, Raper JA. Effect of design on the performance of a dry powder inhaler using computational fluid dynamics. Part 2: air inlet size. J Pharm Sci. 2006;95(6):1382–92.
5. Coates MS, Chan H-K, Fletcher DF, Chiou H. Influence of mouthpiece geometry on the aerosol delivery performance of a dry powder inhalation. Pharm Res. 2007;24(8):1450–6.
6. Shur J, Lee SL, Adams W, Lionberger R, Tibbatts J, Price R. Effect of device design on the in vitro performance and comparability for capsule-based dry powder inhalers. AAPS J. 2012;14(4):667–76.
7. Farkas D, Hindle M, Longest PW. Efficient nose-to-lung aerosol delivery with an inline DPI requiring low actuation air volume. Pharm Res. 2018;35(10):194.
8. Longest PW, Farkas D. Development of a new inhaler for high-efficiency dispersion of spray-dried powders using computational fluid dynamics (CFD) modeling. AAPS J. 2018;21:25. https://doi.org/10.1208/s12248-018-0281-y.
9. Longest PW, Farkas D, Bass K, Hindle M. Use of computational fluid dynamics (CFD) dispersion parameters in the development of a new DPI actuated with low air volumes. Pharm Res. 2019;36(8).
10. Chen X, Zhong W, Zhou X, Jin B, Sun B. CFD–DEM simulation of particle transport and deposition in pulmonary airway. Powder Technol. 2012;228:309–18.
11. Tong Z, Zhong W, Yu A, Chan H-K, Yang R. CFD–DEM investigation of the effect of agglomerate–agglomerate collision on dry powder aerosolisation. J Aerosol Sci. 2016;92:109–21.
12. Yang J, Wu C-Y, Adams M. Three-dimensional DEM–CFD analysis of air-flow-induced detachment of API particles from carrier particles in dry powder inhalers. Acta Pharm Sin B. 2014;4(1):52–9.
13. Ariane M, Sommerfeld M, Alexiadis A. Wall collision and drug-carrier detachment in dry powder inhalers: using DEM to devise a sub-scale model for CFD calculations. Powder Technol. 2018;334:65–75.
14. Wong W, Fletcher DF, Traini D, Chan HK, Young PM. The use of computational approaches in inhaler development. Adv Drug Deliv Rev. 2012;64(4):312–22.
15. Matsui H, Grubb BR, Tarran R, Randell SH, Gatzy JT, Davis CW, et al. Evidence for periciliary liquid layer depletion, not abnormal ion composition, in the pathogenesis of cystic fibrosis airways disease. Cell. 1998;95(7):1005–15.

16. Tarran R, Grubb BR, Parsons D, Picher M, Hirsh AJ, Davis CW, et al. The CF salt controversy: in vivo observations and therapeutic approaches. Mol Cell. 2001;8(1):149–58.

17. Stoltz DA, Meyerholz DK, Welsh MJ. Origins of cystic fibrosis lung disease. N Engl J Med. 2015;372(4):351–62.

18. Elborn JS. Cystic fibrosis. Lancet. 2016;388(10059):2519–31.

19. Smith AL. Inhaled antibiotic therapy: what drug? What dose? What regimen? What formulation? J Cyst Fibros. 2002;1(Suppl 2):189–93.

20. Ramsey BW, Pepe MS, Quan JM, Otto KL, Montgomery AB, Williams-Warren J, et al. Intermittent administration of inhaled tobramycin in patients with cystic fibrosis. N Engl J Med. 1999;340(1):23–30.

21. Farkas D, Hindle M, Bass K, Longest PW. Development of an inline dry powder inhaler for oral or trans-nasal aerosol administration to children. Journal of Aerosol Medicine and Pulmonary Drug Delivery. 2019;In review.

22. Below A, Bickmann D, Breitkreutz J. Assessing the performance of two dry powder inhalers in preschool children using an idealized pediatric upper airway model. Int J Pharm. 2013;444(1–2):169–74.

23. Lindert S, Below A, Breitkreutz J. Performance of dry powder inhalers with single dosed capsules in preschool children and adults using improved upper airway models. Pharmaceutics. 2014;6:36–51.

24. Laube BL, Sharpless G, Shermer C, Sullivan V, Powell K. Deposition of dry powder generated by solovent in Sophia anatomical infant nose-throat (SAINT) model. Aerosol Sci Technol. 2012;46:514–20.

25. Janssens HM, de Jongste JC, Fokkens WJ, Robben SG, Wouters K, Tiddens HA. The Sophia anatomical infant nose-throat (Saint) model: a valuable tool to study aerosol deposition in infants. J Aerosol Med. 2001;14(4):433–41.

26. Son Y-J, Longest PW, Hindle M. Aerosolization characteristics of dry powder inhaler formulations for the excipient enhanced growth (EEG) application: effect of spray drying process conditions on aerosol performance. Int J Pharm. 2013;443:137–45.

27. Son Y-J, Longest PW, Tian G, Hindle M. Evaluation and modification of commercial dry powder inhalers for the aerosolization of submicrometer excipient enhanced growth (EEG) formulation. Eur J Pharm Sci. 2013;49:390–9.

28. ICRP. Human respiratory tract model for radiological protection. New York: Elsevier Science Ltd; 1994.

29. Behara SRB, Longest PW, Farkas DR, Hindle M. Development of high efficiency ventilation bag actuated dry powder inhalers. Int J Pharm. 2014;465:52–62.

30. Bass K, Longest PW. Recommendations for simulating microparticle deposition at conditions similar to the upper airways with two-equation turbulence models. J Aerosol Sci. 2018;119:31–50. https://doi.org/10.1016/j.jaerosci.2018.02.007.

31. Longest PW, Holbrook LT. In silico models of aerosol delivery to the respiratory tract - development and applications. Adv Drug Deliv Rev. 2012;64:296–311.

32. Longest PW, Vinchurkar S. Effects of mesh style and grid convergence on particle deposition in bifurcating airway models with comparisons to experimental data. Med Eng Phys. 2007;29(3):350–66.

33. Longest PW, Son Y-J, Holbrook LT, Hindle M. Aerodynamic factors responsible for the deaggregation of carrier-free drug powders to form micrometer and submicrometer aerosols. Pharm Res. 2013;30:1608–27.

34. Longest PW, Vinchurkar S. Validating CFD predictions of respiratory aerosol deposition: effects of upstream transition and turbulence. J Biomech. 2007;40(2):305–16.

35. Wilcox DC. Turbulence modeling for CFD. 2nd ed. California: DCW Industries, Inc; 1998.

36. Longest PW, Hindle M, Das Choudhuri S, Byron PR. Numerical simulations of capillary aerosol generation: CFD model development and comparisons with experimental data. Aerosol Sci Technol. 2007;41(10):952–73.

37. Longest PW, Vinchurkar S, Martonen TB. Transport and deposition of respiratory aerosols in models of childhood asthma. J Aerosol Sci. 2006;37:1234–57.

38. White FM. Viscous fluid flow. 2nd ed. New York: McGraw-Hill; 1991. xxi, 614 p. p

39. Bhattacharjee S, Grosshandler W, editors. The formation of a wall jet near a high temperature wall under microgravity environment. ASME 1988 National Heat Transfer Conference, Volume 1; 1988.

40. Golshahi L, Noga ML, Thompson RB, Finlay WH. In vitro deposition measurement of inhaled micrometer-sized particle in extrathoracic airways of children and adolescents during nose breathing. J Aerosol Sci. 2011;42:474–88.

41. Javaheri E, Golshahi L, Finlay W. An idealized geometry that mimics average infant nasal airway deposition. J Aerosol Sci. 2013;55:137–48.

42. Storey-Bishoff J, Noga M, Finlay WH. Deposition of micrometer-sized aerosol particles in infant nasal airway replicas. Aerosol Sci. 2008;39:1055–65.

43. Tavernini S, Church TK, Lewis DA, Noga M, Martin AR, Finlay WH. Deposition of micrometer-sized aerosol particles in neonatal nasal airway replicas. Aerosol Sci Technol. 2018;52(4):407–19.

PUBLISHER'S NOTE